optica

Integrated nanophotonic wavelength router based on an intelligent algorithm

Zhouhui Liu,[1,†] Xiaohong Liu,[1,2,†] Zhiyuan Xiao,[1,†] Cuicui Lu,[1,*] [ID] Hui-Qin Wang,[2] You Wu,[3] Xiaoyong Hu,[3,5] Yong-Chun Liu,[4] [ID] Hongyu Zhang,[1] AND Xiangdong Zhang[1,6]

[1]*Beijing Key Laboratory of Nanophotonics and Ultrafine Optoelectronic Systems, School of Physics, Beijing Institute of Technology, Beijing 100081, China*
[2]*Physics Department, School of Sciences, Nanchang University, Nanchang 330031, China*
[3]*State Key Laboratory for Mesoscopic Physics & Department of Physics, Collaborative Innovation Center of Quantum Matter, Beijing Academy of Quantum Information Sciences, Nano-optoelectronics Frontier Center of Ministry of Education, Peking University, Beijing 100871, China*
[4]*State Key Laboratory of Low-Dimensional Quantum Physics, Department of Physics, Frontier Science Center for Quantum Information, Collaborative Innovation Center of Quantum Matter, Tsinghua University, Beijing 100084, China*
[5]*e-mail: xiaoyonghu@pku.edu.cn*
[6]*e-mail: zhangxd@bit.edu.cn*
Corresponding author: cuicuilu@bit.edu.cn

Nanophotonic wavelength routers, which can separate and steer different incident optical wavelengths into different output ports, play a key role in many applications of integrated photonic devices. We design and experimentally demonstrate ultrasmall broadband wavelength routers using an intelligent algorithm that combines a genetic algorithm and the finite element method. The size of the device is only 1.4 μm × 1.8 μm, around the optical communication range, and is the smallest one demonstrated experimentally. The maximum transmission is 98% in the simulation and 71% in the experiment. Moreover, we show that various wavelength routers with different materials (both dielectric and metal), different structures, different output ports, and different operation bands can be conveniently designed using the intelligent algorithm. The average position error tolerance for each cell structure is about ±20 nm for all the wavelength routers designed by our intelligent algorithm, which is possible with current nanofabrication technology. This work provides a universal platform for the realization of nanophotonic wavelength routers, and enables the design and integration of nanophotonic devices. © 2019 Optical Society of America under the terms of the OSA Open Access Publishing Agreement

https://doi.org/10.1364/OPTICA.6.001367

1. INTRODUCTION

Integrated nanophotonics, which takes photons as information carriers, is widely used in optical communication, optical information processing, optical computing, etc. [1–4]. A nanophotonic wavelength router, which can separate and steer different incident optical wavelengths into different output ports, is an essential component for photonic integration. Typical traditional wavelength routers were designed on the basis of structures including optical microcavities, photonic crystals, gratings, metal plasmonic structures, etc. The wavelength routers designed by using microcavities could achieve high efficiency, but the operation bandwidth was narrow [5,6]. In contrast, the routers designed by using photonic crystal and grating generally possessed broad operation band, but the large size restricted their practical integration applications [7–9]. The routing devices based on surface plasmon polaritons possessed a smaller footprint, but suffered high loss [6,10].

With the development of information technology, the requirements for the degree of integration are becoming higher and

higher, including smaller size, broader band, and lower loss of individual optical devices. However, in order to meet the above requirements, traditional design methods were challenged. The design process based on the traditional wavelength routers requires a large amount of computation resource and long time when optimizing the structure parameters, and the optimization process suffered serious limitations [1,2]. An alternative solution is to design intelligent photonic devices by using mathematical optimization algorithms [1–4,11–21]. Among them, the genetic algorithm (GA) as a typical optimization method has attracted great attention for realization of various nanophotonic devices [12–18]; however, nanophotonic wavelength routers based on GA have not been reported. Recently, a method of inverse design has been proposed to realize wavelength routers [19,20]. Piggott *et al.* designed a two-channel wavelength router (or say, wavelength demultiplexer) with a footprint of 2.8 μm × 2.8 μm using inverse design; subsequently, Su *et al.* realized a three-channel wavelength router with a footprint of 5.5 μm × 4.5 μm with the same method [19,20]. However, some very small components

in structures may be formed during the inverse designing process, which brings challenges for current fabrication technology. How to further reduce device size and maintain preparation accuracy simultaneously is a big problem. To date, few reports have been found on integrated wavelength routers with a structure size smaller than 2 μm × 2 μm in the infrared light range; moreover, it is still a great challenge to find a highly efficient design method for wavelength routers applicable for different materials, different configurations, different channels, etc., simultaneously. This has seriously limited the universal design and practical applications of nanophotonic wavelength routers.

In this work, we design and experimentally demonstrate ultra-small broadband wavelength routers for integration realized by using an intelligent algorithm (IA) that combines the GA and the finite element method (FEM). The advantages are mainly as follows. First, the footprint of the wavelength router in the experiment is only 1.4 μm × 1.8 μm around the optical communication range. This is the smallest one ever demonstrated experimentally, which benefits from the fact that the structure size can be preset in our IA. Second, broad operation band, transmission up to 98%, and various output ports can be simultaneously achieved, which benefits from the highly efficient multiobjective optimization generated by the excellent evaluation functions and real-time data exchange between GA and FEM. Third, it is convenient to realize various wavelength routers with different materials (both dielectric and metal), different configurations, different channels, different structure cell quantities, or size due to the good applicability of our IA. In addition, the average position error tolerance for each cell structure is about ±20 nm for all the wavelength routers designed by our IA, which satisfies current nanofabrication technology. This paves a way for the practical applications of integrated nanophotonic devices.

2. DESIGN METHOD

The building process for the IA by combining the GA and the FEM is shown in Fig. 1(a). First, we consider a planar binary structure composed of two different materials with different refractive indices, both dielectric and metal. The structure is composed of some basic cells. It is worth mentioning that the cells can be set with specified or arbitrary shapes, such as squares, rectangles, circles, and triangles, etc., so we can control the cell size within our fabrication capacity. When light propagates through the structures, the electromagnetic field distributions will be changed with the changes of the cells' distribution. Thus, the distribution of cells is described as a design variable, and each channel's transmittance is regarded as an optimization objective that indicates the performance of the device. In the flow chart of Fig. 1(a), a random initial population is created as the first generation in step ①, which contains many different models with different irregular arranged structures. In step ②, the FEM computing and the GA coding operate simultaneously and realize timely data exchange so that we can adjust the structure conveniently. In step ③, GA gets the electromagnetic field response solved by FEM and evaluates the individual's fitness, where the value of fitness function [see Supplement 1, Section 1, Eq. (S3)] represents the expected goal. In step ④, sort the population by fitness. The population's binary code with higher fitness is of higher opportunity to be selected as the parent generation. In step ⑤, GA creates a child generation code through the new combination of parent code after crossover and mutation. Correspondingly, new structures with improved performances are generated by FEM. The loop will not complete until meeting the user's objectives, i.e., the convergence condition is reached (see Supplement 1, Section 1 for more information about selection, crossover, mutation, and convergence condition). The structure changes during the iterative computing process, and the corresponding output results are shown in Fig. 1(b). The upper structure is an initial model of the first generation, which usually possesses low fitness. The middle structure is the nearly half-optimized individual that shows a component with new distribution and higher fitness. After iterating more generations through crossover and mutation, an optimized nanophotonic router that reaches the convergence condition will be obtained, shown in the lower structure, where the incident wavelengths are separated and steered into specific channels. This is the main designing process for nanophotonic wavelength routers.

In the general optimization process, it will take plenty of time due to the expanded freedom space if many parameters need to be determined simultaneously. In our IA, we can save time cost by presetting cell size or shapes and obtaining the real-time data exchange between GA and FEM. We can optimize different routers with appropriate structures and befitting channels to meet various requirements, presenting good applicability. Meanwhile, we present a smart objective function to describe these variables, which contains the harmonic mean and root-mean-square error employed to balance the intensity of optimized signals and inhibited noise. The advantage is that it guarantees high enough signal intensity and, meanwhile, insures adequately low-level noise. Besides, the objective function provides a strong optimization guidance, leading to an efficient design cycle. More details about the feature of IA and the objective function are expatiated in Sections 1.A and 1.B of Supplement 1, respectively. Due to the fact that the analysis in GA only relies on the electromagnetic field response of FEM rather than the multiple variables, through the real-time data exchange between GA and FEM, optimization time does not increase even if the variables or objectives increase.
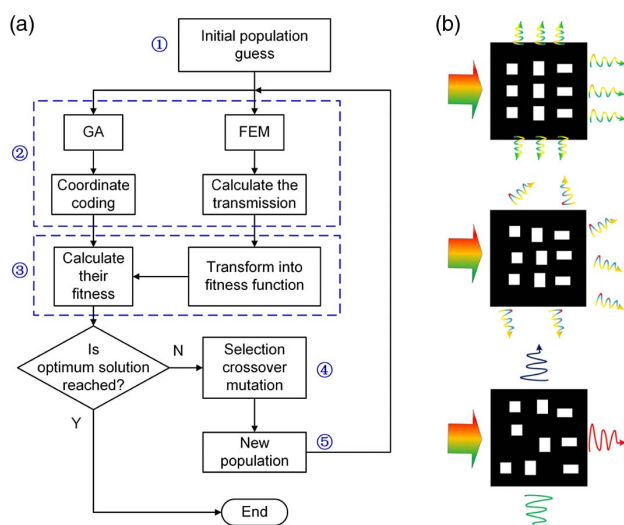

Fig. 1. IA method. (a) Flow chart of IA; (b) structural changes during iteration. Three graphs in order: the initial individual, the nearly half-optimized individual, the final optimized individual. The black area indicates material 1, and the white area denotes material 2.

The IA can be employed in ordinary computers with typical equipment. Here we give an example of the calculation time for a two-dimensional (2D) model with an area of 1.5 μm × 1.5 μm in detail. The FEM calculation is based on the commercial solver of COMSOL Multiphysics, and GA operates in MATLAB. The final structure is designed with the population size of 30, after 200 iterations, in about only 3 h using a personal computer with 4 Intel (R) Core (TM) i7-7500U CPU at 2.7 GHz, and 8 GB installed memory (RAM, random access memory).

3. VARIOUS ROUTER DESIGNS

A. Two-Channel Wavelength Router of Metal Material

First, we design a two-channel wavelength router by using silver embedded in air. The device geometry is shown in Fig. 2(a). The wavelength-dependent complex refractive index function of silver is taken from Ref. [22]. The design region occupies a 1.0 μm × 1.0 μm footprint, where 4 × 4 silver rectangles are in the area before optimization. We give the algorithm intelligence to filter out the newly created structural unit, which is too small. The width of the input and output ports are all 500 nm. The input port (In) is on the center of the left boundary, while the output ports are on upper center (O1) and lower center (O2). In the design, the object center wavelengths are set to be 580 and 805 nm with a near-Gaussian line shape, and other wavelength ranges are inhibited. The width, height, and the position of the center of each rectangle are set as variables. Then, we determine all the variables using the algorithm. The calculated transmission spectrum is shown in Fig. 2(b). When the TM-polarized light with a range of 480 to 950 nm is incident to the left input port, only the center wavelength of 580 and 805 nm channels can transmit through the output ports, where the full width at
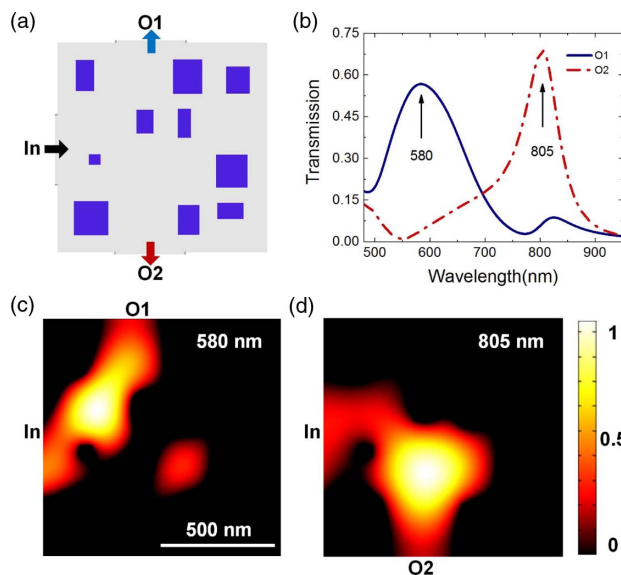
half-maximum (FWHM) is 156 and 82 nm, respectively, which can be used for wide-channel light routing with an ultracompact footprint. The corresponding simulated electric fields of the two wavelengths are plotted in Figs. 2(c) and 2(d). It is very clear that the electromagnetic waves for wavelengths 580 and 805 nm propagate into different output ports, respectively. The transmittance of the two channels are 57% and 69%, respectively, and we get low cross talk, meaning that it successfully filters the noise we set. The maximum length of all the rectangles is about 160 nm, while the minimum is about 60 nm, which is within the nanofabrication capacity. The final structure is designed after 200 iterations in about 3 h using a personal computer with 4 Intel (R) Core (TM) i7-7500U CPU at 2.7 GHz, and 8 GB installed memory (RAM). It is worth mentioning that the performance of devices can be further improved with the increase of iteration times and time extension.

In addition, the wavelength router based on the silver/air materials can be extended from two channels to three channels or even more, only if we set more output ports in our IA without more calculation time cost. When the TM-polarized light with a range of 350 to 1100 nm is incident to the left input port, three channels with the center wavelength of 450, 600, and 800 nm could support the transmission of the wave through the output ports, respectively, which was shown in Section 2.A (Fig. S1) of Supplement 1.

B. Three-Channel Router of Dielectric Material

The developed IA can also be used to design routers with more channels and different materials. A three-channel wavelength router based on silicon/air is further achieved using the IA. The final optimized geometry is indicated in Fig. 3(a). The design footprint is 1.5 μm × 1.5 μm, where the 5 × 5 initial silicon squares are placed, and the size of each is 140 nm × 140 nm. The number of squares is a fixed parameter, or a variable can

Fig. 2. Two-channel wavelength router for metal materials. (a) Structure of the router. The blue holes are silver and the white area is filled with air. The size of the structure is 1.0 μm × 1.0 μm. (b) Simulated transmission spectrum covering from 480 to 950 nm. The transmission peaks are $\lambda = 580$ nm and $\lambda = 805$ nm, respectively. In denotes input port; O1, O2 are the upper output port and the lower output port, respectively. (c) and (d) The simulated magnitude of the electric field at 580 and 805 nm, respectively.
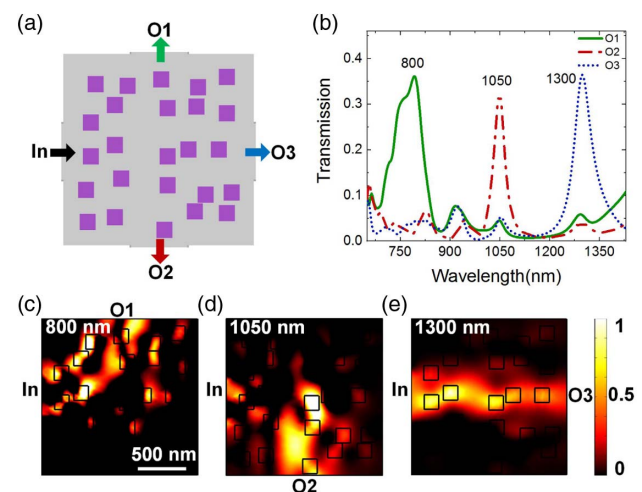

Fig. 3. Three-channel wavelength router. (a) Structure of the router. The light gray area indicates silicon dioxide, the purple rectangle denotes silicon. The size of the structure is 1.5 μm × 1.5 μm. (b) Simulated transmission spectrum covering from 650 to 1500 nm, where the peaks corresponding to the wavelength of 800, 1050, and 1300 nm. In denotes input port; O1, O2, and O3 are the upper output port, the lower output port, and the right output port. (c)–(e) Simulated power flow on time average at 800, 1050, and 1300 nm, respectively.

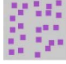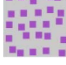be preset. Both the number and the size of the scatters are fixed in this design. The purple rectangle denotes silicon, and the gray area indicates silicon dioxide, where $n_{si} = 3.45$ and $n_{sio2} = 1.45$. Compared to the first model of two-chan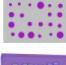nel wavelength router, we add one output port and adjust their position to upper center (O1), lower center (O2) and righte center (O3) of the boundaries, respectively. Besides optimization objects for the center wavelengths of 800, 1050, and 1300 nm with a near-Gaussian line shape, other wavelength ranges are set to be inhibited. The calculated transmission spectra are shown in Fig. 3(b). When TM-polarized light with a range of 650–1500 nm is incident to the left input port, only channels with the center wavelengths of 800, 1050, and 1300 nm can support transmission of the wave through the output ports, where the FWHM is 90, 39, and 70 nm, respectively. The transmission for each channel is 37%, 33%, and 36%, respectively, and the cross talk is very low. The transmission of the wavelength range between the neighboring channels is filtered, so that the router performs strong anti-interference capability and ensures the reliability of signal transmission for each channel. We plot the corresponding simulated power flow on time average of the device surface, shown in Figs. 3(c)–3(e). It is shown clearly that the electromagnetic waves for wavelengths 800, 1050, and 1300 nm propagate into different output ports, respectively. In fact, the operation band and the center wavelength can be easily tuned in our IA. We have designed some other two-channel and three-channel wavelength routers. They possess different output ports, different materials, and different structures, which are shown in Sections 2.B, 2.C, and 2.D of Supplement 1. The main performance of the nanophotonic wavelength routers is further given in the following section.

C. Comparisons and Summaries for Wavelength Routers

In order to explore the size limit and to suit practical applications in different cases of wavelength routers, we designed a variety of nanophotonic wavelength routers with different materials, different structure cells, and different operation bands based on our IA. These nanophotonic wavelength routers possess excellent performance designed by the IA.

The comparisons and summaries for wavelength routers are shown in Table 1. These data display the performance of our devices visually. All of the structure sizes of all wavelength routers are less than 2 µm × 2 µm, of which the smallest one is 1 µm× 1 µm, and the one used in the experiment is 1.4 µm × 1.8 µm. The operation band can cover from visible light to infrared light, the transmission of 3D model is 98%, the maximum transmission of 2D models is 79%, and we realize different wavelength routers with different materials (no matter whether they are dielectric or metal), different structures, and different cell quantities, which paves the way for practical applications. It is also found that the wavelength router with a triangle-shaped cell structure possesses higher transmission among the 2D models, since the localized modes are easy to form due to the sharp boundary of the cell structure. In addition, in order to verify the robustness of devices designed by the IA, we calculate the position error tolerance of each structure cell, which is shown in the last column of Table 1. The 2D (Fig. 2), 2D (Fig. 3), and 3D (Fig. 5) correspond to Fig. 2, Fig. 3, and Fig. 5 in the text, respectively. The 2D (Fig. S1), 2D (Fig. S2), 2D (Fig. S3), 2D (Fig. S4), 2D (Fig. S5), and 2D (Fig. S6) correspond to Fig. S1, Fig. S2, Fig. S3, Fig. S4, Fig. S5, and Fig. S6 in Supplement 1, respectively.

Table 1. Performance Comparison of Designed Various Wavelength Routers

Types	Structure	Size (µm²)	Output Center Wavelengths (nm)	Center Wavelengths Transmittances	Materials	Position Error Tolerance
2D (Fig. 2)		1.0 × 1.0	2 ports; 580; 805	57%; 69%	Silver/Air	±17 nm
2D (Fig. S1)		1.1 × 1.1	3 ports; 450; 600; 800	34%; 34%; 53%	Silver/Air	±14 nm
2D (Fig. 3)		1.5 × 1.5	3 ports; 800; 1050; 1300	37%; 33%; 36%	Si/SiO₂	±21 nm
2D (Fig. S2)		1.5 × 1.5	2 ports; 1300; 1550	38%; 29%	Si/SiO₂	±30 nm
2D (Fig. S3)		2.0 × 2.0	2 ports; 1050; 1300	40%; 40%	Si/SiO₂	±15 nm
2D (Fig. S4)		2.0 × 2.0	3 ports; 1050; 1300; 1550	37%; 43%; 39%	Si/SiO₂	±28 nm
2D (Fig. S5)		1.9 × 1.9	3 ports; 790; 1200; 1550	77%; 79%; 67%	Si/Air	±10 nm
2D (Fig. S6)		1.5 × 1.5	3 ports; 800; 1200; 1550	53%; 36%; 29%	Si/SiO₂	±21 nm
3D (Fig. 5)		1.4 × 1.8	3 ports; 1180; 1460; 1700	92%; 98%; 84%	Air/Si/SiO₂	±25 nm

The position error tolerance is defined as the maximum distance shift for each cell. For each structure, we moved the position of all the holes or pillars randomly within a certain distance and calculated the transmission spectra of wavelength routers. For all the devices, we made uniform standards for the error tolerance. It was considered to be acceptable for the devices only if the center wavelength shifts did not exceed 50 nm (about 3% for the infrared light and 6% for the shorter wavelength of designed routers), the relative decrease of the maximum transmission did not exceed 0.1, and the absolute increase of the maximum value of noise for each wavelength did not exceed 0.1. For each distance and each device, we repeated the process more than 20 times; if the performances of the randomly changed structure came up to the above standards every time, then we thought the error was acceptable. The position error tolerance of each cell structure is up to ± 30 nm for the two-channel router with a footprint of 1.5 μm × 1.5 μm, separating 1300 and 1550 nm based on silicon/silicon dioxide materials. The transmission spectrum changes with the tolerance increase for every 5 nm (from ± 10 nm to ± 35 nm) are shown in Supplement 1 (see Section 2.G, Fig. S7 in Supplement 1). It is found that the cell structure with the triangle-type possesses a smaller position error tolerance (± 10 nm) than other shapes of cell structures. The average position error tolerance is about ± 20 nm for various nanophotonic wavelength routers designed by our IA, which completely satisfies current nanofabrication technology. In addition, the bandwidth can be improved by changing the number or shape of cells and the size of devices or materials.

Here we also give theoretical illustrations for the wavelength routers. In the electronic systems, a classical theory of particle propagation in disordered media, which is called Anderson localization, was first proposed by Anderson [23]. Electrons are diffused when they propagate in an ordered regular array. Anderson introduced a random potential energy in the regular array to form a disordered lattice with random distribution. Specifically, when the random potential energy changes greatly and reaches a certain critical value, electrons are localized to a specific position. In our photonic system, photon localization is analogous to electrons [24–26]. Each structure cell can be considered as an optical scatter, which results in multiple scattered waves [27,28]. When the multiple scattered optical waves interfere with each other, the electromagnetic waves form a variety of localized modes and guided modes in the structure obtained by IA [27]. The localized modes are generally trapped in the structure, while the guided modes can form microchannels for light transmission. When the incident light wavelengths match the guide modes, they can transmit through the structure; however, if the incident wavelengths do not match the guide modes, the incident light waves will be forbidden. Therefore, the transmission for different incident wavelengths and different structures will be different.

4. EXPERIMENTAL RESULTS

Assuming more time consumption for the three-dimensional (3D) model than for the 2D model, we establish an equivalent 2D model for 3D model by using the effective refractive index method. The effective refractive index method is widely used in the design of nanophotonic devices [6,29–31]. We use the means of 2D mode analysis to calculate the effective refractive index of the TE mode used in the 3D model, as shown in

Fig. 4(a), where the upper layer is air with a thickness of 2000 nm, the middle layer is silicon with a thickness of 220 nm, and the lower layer is SiO_2 with a thickness of 1500 nm. The obtained effective refractive index is 2.8 by using mode analysis. Then we calculated the transmission spectrum of the output ports for the 2D model and the 3D model of the wavelength routers. The simulated transmission line shapes of the equivalent 2D model are almost in agreement with that of the 3D model by using the effective refractive index method (see Section 3 in Supplement 1). The difference is that the transmittance of the 2D model is lower than that of the 3D model because the 2D model is infinitely long in the z axis, the 3D model has a certain thickness, and the radiant power of the 2D model is more than that of the 3D model. The 3D structure model for wavelength router is shown in Fig. 4(b), where the substrate material is silicon dioxide, the purple area represents silicon, the materials of small cuboids are all air, the footprint of the device is only 1.4 μm × 1.8 μm, and the size of the inner rectangle is 100 nm × 200 nm.

The sample fabrication process is as follows. We etched on the silicon-on-insulator (SOI) plate by using the scanning electron microscopy (SEM)/focused ion beam (FIB) system (FEI Helios NanoLab 600i). For the purpose of experiment, etched structures include the rectangle air hole area, coupling ports and waveguides, as well as corresponding reference samples. The SEM images of the etched sample and reference are shown in Fig. 4(c) and Fig. 4(d), respectively. The left figure is the front view of the complete structure and the reference structure. The right is the enlarged structure and reference structure picture. The etched beam of the central device is 30 kV and 7.7 pA, and the etched
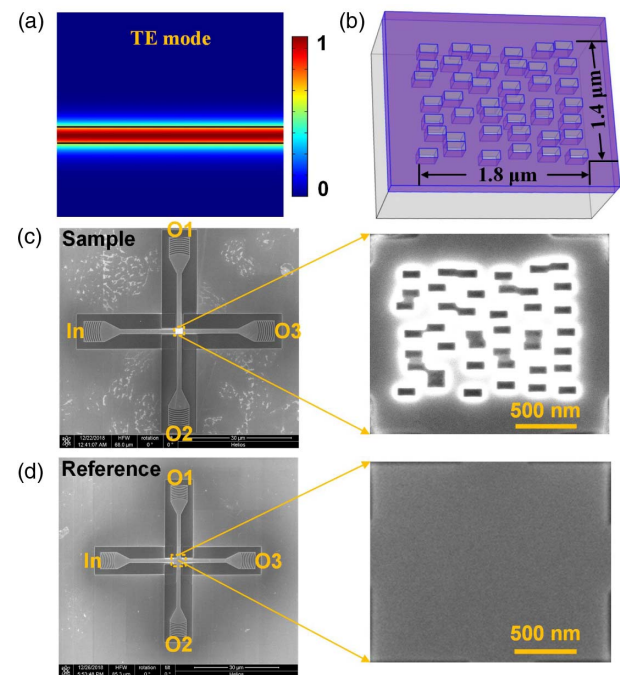

Fig. 4. (a) Electric field distribution of the TE mode. (b) 3D model of the structure. (c) and (d) Top view of the SEM images of the sample and reference sample. The left is the overall structure diagram, and the right is the enlarged image of the footprints for the device structure and reference structure, respectively. In denotes input port; O1, O2, and O3 are the upper output port, the lower output port, and the right output port, respectively.

beam of the coupling ports and waveguides are 30 kV and 80 pA. Moreover, the size of coupling ports is 6 μm × 6 μm, whose center structures are arc-shaped grating, the arc-shaped grating period is 600 nm, the radius of the circle is 6.9 μm, and the depth of the arc-shaped grating is 110 nm. The maximum excitation efficiency of the coupling port reaches 12%. The length of the waveguides is 20 μm. The left and right port lengths of the trapezoidal waveguide are 6 μm and 500 nm, respectively.

The established optical fiber-coupled experimental system is shown in Fig. 5(a). The diameter of the optical fiber taper used is about 125 μm. In order to obtain the intensity from the decoupling ports directly, we used the flame-heated drawing technique to stretch the diameter of the optical fiber to 4 μm. In the measurement, we used a supercontinuum wave (SCW) laser (SC-5, YSL) to provide signal optical excitation, and a spectrometer (model Andor 303i) to measure the wavelength distribution of the three ports. As the detection range of the spectrometer is limited in the near-infrared band, which can only be set up to about 130 nm at a time, the full routing range cannot be measured at once. Therefore, we measured transmission spectra of the three ports in a segmented manner to obtain the final data. The specific test steps are as follows. First, find the position of the sample under the optical microscope, adjust it to the optimal field of vision, adjust the stretched fiber to the position of the input port and output port, adjust the polarizer, and measure the background; second, turn on the laser, set the center wavelength of the corresponding output port in the spectrometer software, and obtain the measured spectrum. Each output port of the samples and their references was tested through the above steps.

The normalized transmission spectrum is the ratio of the measured intensity of patterned sample to the unpatterned sample, so as to eliminate the influences of different wavelengths of the laser source, the coupling efficiencies of gratings, and the sensitivities of the spectrum, which is a general method for the measured results [32,33]. In the theoretical calculations, the normalized transmission is the ratio of the transmittance at the three ports of the router to the transmittance at the port-O3 of reference. Therefore, the normalized transmission of the experiment is the ratio of the spectrum intensity measured at the three ports of the router to the spectrum intensity measured at the port-O3 of reference. The measured experimental results are shown in Fig. 5(b). The center wavelengths of the output ports are 1180, 1460, and 1700 nm, and the measured corresponding transmittances of the center wavelengths are 65%, 71%, and 45%, respectively. The simulated transmission spectrum is shown in Fig. 5(c). The generated routing structure achieves the highest transmittance of 98% at 1460 nm in 3D simulation, and the transmittance at 1180 and 1700 nm reaches 92% and 84%, respectively. It can be seen that the experimental and theoretical line shapes are in agreement, and the center wavelengths are also in agreement. The experimental transmittance is lower than that of the theoretical calculations; it mainly results from the losses in the experiment. Due to the imperfect fabrication of the FIB etching technique, the inner wall is rough, the corner of the rectangle hole is some fillet, and the diameter of the holes becomes smaller from top to bottom. In addition, some TM modes may also be excited by using the grating couplers, though they are very weak. The transmission for the excited TM modes is larger for the reference samples without holes than that of the sample with etched holes. The above factors mainly cause the transmittance to be lower in the experiment. The bandwidth of the transmission spectrum in the experiment is narrower than that in theory. For this, the bandwidth can be improved by improving the processing accuracy and suppressing the background noise to improve the signal strength as much as possible.

5. CONCLUSION

In conclusion, we have realized an ultrasmall broadband wavelength router for integration through an IA by combining the GA and FEM. The size of the device is only 1.4 μm × 1.8 μm around the optical communication range, which is the smallest silicon-based wavelength router. The maximum transmission is 98% in the simulation and 71% in the experiment. It is also very convenient to realize different wavelength routers with different materials (no matter whether they are dielectric or metal), different structures, different cell quantities, or size due to the good applicability of our method. The average error tolerance is about ±20 nm for the wavelength routers designed by our IA, which satisfies current nanofabrication technology. This work provides a new method for the universal design of nanophotonic wavelength routers, and will greatly promote the development of nanophotonic integrated devices, as well as future applications in highly integrated photonic chips.

See Supplement 1 for supporting content.

†These authors contributed equally to this work.

Fig. 5. (a) Experimental setup; (b) measured transmission spectrum; (c) calculated transmission spectrum. The green solid, red dotted-dashed and blue dashed lines correspond to the top, bottom, and right output ports, respectively, and the wavelength range is from 1050 to 1950 nm.

REFERENCES

1. S. Molesky, Z. Lin, A. Y. Piggott, W. Jin, J. Vucković, and A. W. Rodriguez, "Inverse design in nanophotonics," Nat. Photonics **12**, 659–670 (2018).
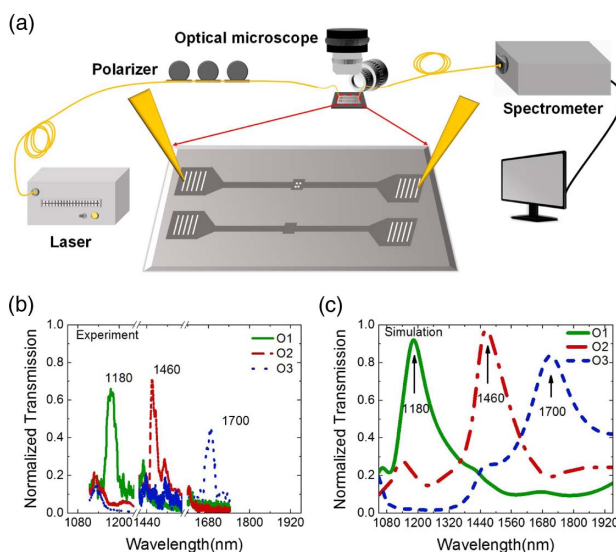
2. K. Yao, D. R. Unni, and Y. Zheng, "Intelligent nanophotonics: merging photonics and artificial intelligence at the nanoscale," Nanophotonics **8**, 339–366 (2019).

3. B. Shen, P. Wang, R. Polson, and R. Menon, "Ultra-high-efficiency meta-material polarizer," Optica **1**, 356–360 (2014).

4. B. Shen, P. Wang, R. Polson, and R. Menon, "An integrated-nanophotonics polarization beamsplitter with 2.4 × 2.4 μm2 footprint," Nat. Photonics **9**, 378–382 (2015).

5. J. Ferrera, G. Steinmeyer, L. C. Kimerling, E. R. Thoen, J. S. Foresi, J. D. Joannopoulos, P. R. Villeneuve, S. Fan, E. P. Ippen, and H. I. Smith, "Photonic-bandgap microcavities in optical waveguides," Nature **390**, 143–145 (1997).

6. C. Lu, Y. Liu, X. Hu, H. Yang, and Q. Gong, "Integrated ultracompact and broadband wavelength demultiplexer based on multi-component nano-cavities," Sci. Rep. **6**, 27428 (2016).

7. O. M. Nawwar, H. Shalaby, and R. K. Pokharel, "Photonic crystal-based compact hybrid WDM/MDM (De)multiplexer for SOI platforms," Opt. Lett. **43**, 4176–4179 (2018).

8. H. Ito, T. Tatebe, H. Abe, and T. Baba, "Wavelength-division multiplexing Si photonic crystal beam steering device for high-throughput parallel sensing," Opt. Express **26**, 26145–26155 (2018).

9. Y. Chen, S. Wang, T. Lang, and J. J. He, "Uniform-loss cyclic arrayed waveguide grating router using a mode-field converter based on a slab coupler and auxiliary waveguides," Opt. Lett. **44**, 211–214 (2019).

10. J. S. Q. Liu, R. A. Pala, F. Afshinmanesh, W. Cai, and M. L. Brongersma, "A submicron plasmonic dichroic splitter," Nat. Commun. **2**, 525 (2011).

11. D. T. Pham and D. Karaboga, *Intelligent Optimisation Techniques* (Springer, 2000), p. 3.

12. S. Forrest, "Genetic algorithms: principles of natural selection applied to computation," Science **261**, 872–878 (1993).

13. J. Goh, I. Fushman, D. Englund, and J. Vucković, "Genetic optimization of photonic bandgap structures," Opt. Express **15**, 8218–8230 (2007).

14. P. R. Wiecha, A. Arbouet, C. Girard, A. Lecestre, G. Larrieu, and V. Paillard, "Evolutionary multi-objective optimization of colour pixels based on dielectric nanoantennas," Nat. Nanotechnol **12**, 163–169 (2017).

15. Z. Jin, S. Mei, S. Chen, Y. Li, C. Zhang, Y. He, X. Yu, C. Yu, J. K. W. Yang, B. Lukyanchuk, S. Xiao, and C. Qiu, "Complex inverse design of meta-optics by segmented hierarchical evolutionary," ACS Nano **13**, 821–829 (2019).

16. Z. Yu, H. Cui, and X. Sun, "Genetic-algorithm-optimized wideband on-chip polarization rotator with an ultrasmall footprint," Opt. Lett. **42**, 3093–3096 (2017).

17. A. C. S. Chan, A. K. S. Lau, K. K. Y. Wong, E. Y. Lam, and K. K. Tsia, "Arbitrary two-dimensional spectrally encoded pattern generation—a new strategy for high-speed patterned illumination imaging," Optica **2**, 1037–1044 (2015).

18. G. Pu, L. Yi, L. Zhang, and W. Hu, "Intelligent programmable mode-locked fiber laser with a human-like algorithm," Optica **6**, 362–369 (2019).

19. A. Y. Piggott, J. Lu, K. G. Lagoudakis, J. Petykiewicz, T. M. Babinec, and J. Vucković, "Inverse design and demonstration of a compact and broadband on-chip wavelength demultiplexer," Nat. Photonics **9**, 374–377 (2015).

20. L. Su, A. Y. Piggott, N. V. Sapra, J. Petykiewicz, and J. Vucković, "Inverse design and demonstration of a compact on-chip narrowband three-channel wavelength demultiplexer," ACS Photon. **5**, 301–305 (2017).

21. J. S. Jensen and O. Sigmund, "Topology optimization for nano-photonics," Laser Photon. Rev. **5**, 308–321 (2011).

22. P. B. Johnson and R. W. Christy, "Optical constants of the noble metals," Phys. Rev. B **6**, 4370–4379 (1972).

23. P. W. Anderson, "Absence of diffusion in certain random lattices," Phys. Rev. **109**, 1492–1505 (1958).

24. T. Schwartz, G. Bartal, S. Fishman, and M. Segev, "Transport and Anderson localization in disordered two-dimensional photonic lattices," Nature **446**, 52–55 (2007).

25. C. Conti and A. Fratalocchi, "Dynamic light diffusion, three-dimensional Anderson localization and lasing in inverted opals," Nat. Phys. **4**, 794–798 (2008).

26. H. H. Sheinfux, Y. Lumer, G. Ankonina, A. Z. Genack, G. Bartal, and M. Segev, "Observation of Anderson localization in disordered nanopho-tonic structures," Science **356**, 953–956 (2017).

27. S. John, "Localization of light," Phys. Today **44**(5), 32–40 (1991).

28. H. Cao, J. Y. Xu, D. Z. Zhang, S. Chang, S. T. Ho, E. W. Seelig, X. Liu, and R. P. Chang, "Spatial confinement of laser light in active random media," Phys. Rev. Lett. **84**, 5584–5587 (2000).

29. C. Lu, X. Hu, H. Yang, and Q. Gong, "Ultrawide-band unidirectional sur-face plasmon polariton launchers," Adv. Opt. Mater. **1**, 792–797 (2013).

30. N. Yokouchi, A. J. Danner, and K. D. Choquette, "Etching depth depend-ence of the effective refractive index in two-dimensional photonic-crystal-patterned vertical-cavity surface-emitting laser structures," Appl. Phys. Lett. **82**, 1344–1346 (2003).

31. S. Dwivedi, A. Ruocco, M. Vanslembrouck, T. Spuesens, P. Bienstman, P. Dumon, T. Van Vaerenbergh, and W. Bogaerts, "Experimental extrac-tion of effective refractive index and thermo-optic coefficients of silicon-on-insulator waveguides using interferometers," J. Lightwave Technol. **33**, 4471–4477 (2015).

32. C. Liguda, G. Böttger, A. Kuligk, R. Blum, M. Eich, H. Roth, J. Kunert, W. Morgenroth, H. Elsner, and H. G. Meyer, "Polymer photonic crystal slab waveguides," Appl. Phys. Lett. **78**, 2434–2436 (2001).

33. C. Lu, X. Hu, H. Yang, and Q. Gong, "Ultrahigh-contrast and wideband nanoscale photonic crystal all-optical diode," Opt. Lett. **36**, 4668–4670 (2011).